

PAPER

View Article Online



Cite this: EES Sol., 2025, 1, 567

Approaching the radiative limits for wide bandgap perovskite solar cells using fullerene blend electron transport interlayers†

Josephine L. Surel, (1) ‡a Pietro Caprioglio, (1) ‡a Joel A. Smith, (1) a Akash Dasgupta, (1) a Francesco Furlan, (1) b Charlie Henderson, (1) c Fengning Yang, (1) a Benjamin M. Gallant, (1) a Seongrok Seo, (1) a Alexander Knight, (1) d Manuel Kober-Czerny, Da Joel Luke, Dc David P. McMeekin, Da Alexander I. Tartakovskii, Dd Ji-Seon Kim, o Nicola Gasparini b and Henry J. Snaith ** **

Performance losses in positive-intrinsic-negative architecture perovskite solar cells are dominated by nonradiative recombination at the perovskite/organic electron transport layer interface, which is particularly problematic for wider bandgap perovskites. Large endeavours have been dedicated to the replacement of fullerenes, which are the most commonly used class of electron transport layers, with limited success thus far. In this work, we demonstrate blending the fullerene derivatives [6,6]-phenyl C₆₁ butyric acid methyl ester (PCBM) and indene- C_{60} bis-adduct (ICBA) as a thin interlayer between 1.77 eV bandgap perovskite and an evaporated C_{60} layer. By tuning the fullerene blend to a trace 2% by mass of PCBM in ICBA, we remarkably form an interlayer which features improved energetic alignment with the perovskite and the PCBM: ICBA fullerene mixture, together with a stronger molecular ordering and an order of magnitude higher electron mobility than either neat PCBM or ICBA. Additional molecular surface passivation approaches are found to be beneficial in conjunction with this approach, resulting in devices with 19.5% steady state efficiency, a fill factor of 0.85 and an open-circuit voltage of 1.33 V, which is within 10% of the radiative limit of the latter two device parameters for this bandgap. This work highlights the complex nonlinear energetic behaviour with fullerene mixing, and how control of the energetics and crystallinity of these materials is crucial in overcoming the detrimental recombination losses that have historically limited perovskite solar cells.

Received 27th June 2025 Accepted 2nd July 2025

DOI: 10.1039/d5el00103j

rsc.li/EESSolar

Broader context

The performance of perovskite-based tandem photovoltaics has progressed remarkably in recent years and promises to help reduce the cost-per-watt of solar energy. Wide bandgap perovskite solar cells are an essential component for tandems, but despite significant improvements in performance and stability, they still suffer from voltage losses, primarily induced by the properties of the perovskite-electron transport layer interface. These losses are largely due to nonradiative recombination caused in part by poor energetic alignment of the perovskite and the transport material. In this work we introduce an interlayer composed of a precisely tuned blend of PCBM and ICBA to energetically align with the wide bandgap perovskite, thereby improving the V_{OC} without sacrificing current flow through the device stack. Unexpectedly, we find that by mixing a very small amount (2% by mass) of PCBM into ICBA we form a material with significantly improved electron mobility, crystallinity, and energetic alignment with a 1.77 eV perovskite absorber layer designed for all-perovskite tandems. When implemented into devices, this translates to reduced nonradiative recombination and improved voltage and fill factor. This work provides insight into the importance of controlling the properties of transport materials, with enhanced crystallinity and charge carrier mobility appearing to be important. It further highlights how blends of organic charge transport materials can deliver functionality beyond what is possible with single component systems. We also demonstrate that our approach can be adapted to multiple perovskite architectures and absorber bandgaps to help enable high performing devices.

Introduction

Metal-halide perovskite solar cells (PSCs) have experienced tremendous improvements in performance over the past decade, with record power conversion efficiency (PCE) now exceeding 26% for a single junction device. 1-3 The remarkable optoelectronic properties of metal halide perovskites, coupled with ease of processing and bandgap tunability, make them

^aDepartment of Physics, University of Oxford, Clarendon Laboratory, Parks Road, Oxford, OX1 3PU, UK. E-mail: henry.snaith@physics.ox.ac.uk

^bDepartment of Chemistry and Centre for Processable Electronics, Imperial College London, London, W12 0BZ, UK

Department of Physics and Centre for Processable Electronics, Imperial College London, London, SW7 2AZ, UK

^dDepartment of Physics and Astronomy, University of Sheffield, Sheffield, S3 7RH, UK † Electronic supplementary information (ESI) available. See DOI: https://doi.org/10.1039/d5el00103j

[‡] These authors contributed equally.

a very promising candidate for commercialization. Bandgap tunability enables multijunction devices to deliver efficiencies beyond the radiative limit of single junction solar cells.4 This will aid in increasing the power density and reducing the overall system cost of solar, making renewable energy a more attractive and accessible option for a variety of sectors. 5,6 "All-perovskite" tandems, constructed from multiple perovskite solar cells with different bandgaps stacked on top of each other, have now reached record efficiencies of >29%.7,8 However, fundamental losses in the wide bandgap (WBG) top cell still inhibit these devices from reaching their maximum potential.

In recent years, progress has been made in developing high performing WBG devices. However, energy losses at the perovskite/electron transport layer (ETL) interface still significantly limit the open-circuit voltage (V_{OC}) of most devices. We recently demonstrated that these energy losses are associated with strong interface recombination due to an energy misalignment between the perovskite and charge transport layers (CTL). This results in the external V_{OC} being lower than the internal "quasi-Fermi level splitting" (QFLS) of the same device, where QFLS is an estimate of the "internal voltage" generated in the perovskite layer under sunlight, and sets a maximum limit to the $V_{\rm OC}$ the solar cell could generate.⁹⁻¹² While at the hole transport layer (HTL) interface there are a large variety of transport materials13 that can be used to mitigate this problem (metal oxides,14 polymers,15 and selfassembled monolayers16), at the electron transport layer (ETL) interface, despite many attempts, 17 fullerenes have been the most successful option so far in positive-intrinsic-negative (pi-n) architecture. Due to this limitation, the non-radiative recombination losses at the perovskite/ETL interface are one of the major limitations of wide-gap perovskite solar cells. 16,18-20

To overcome the $V_{\rm OC}$ losses at the perovskite-ETL interface we investigate the impact of blending fullerene derivatives instead of replacing the fullerene ETL with other electron transport materials.21-23 Khadka et al. showed in 2018 that using chain-substituted fullerene derivatives as the ETL can tailor the performance parameters of WBG PSCs.21 They found particular success in improving the VOC using C60-fused N-methylpyrrolidine-meta-dodecyl phenyl (CMC) due to its improved crystallinity and band alignment with the perovskite when compared with the more commonly used [6,6]-phenyl C₆₁ butyric acid methyl ester (PCBM). Liu et al. extended this strategy and demonstrated that both CMC and indene-C₆₀ bisadduct (ICBA) significantly improve the device $V_{\rm OC}$ compared to PCBM, and when blended in equal amounts achieve an even higher $V_{\rm OC}$ without introducing reductions in short-circuit current (I_{SC}) and fill factor (FF) that occur when using either neat material on its own.22 However, both PCBM and ICBA are more widely available and less expensive (at the lab scale) than CMC,24-26 which provides an advantage when considering scaling up photovoltaic production using PSCs. With this in mind, Sun et al. proposed a scalable strategy blending PCBM, ICBA, and C_{60} . This mixture enabled a 40 mV increase in V_{OC} compared to evaporated C₆₀ as the ETL in small (0.049 cm² aperture area) devices, and ultimately translated to an all-

perovskite tandem module (20.25 cm² aperture area) with a PCE of 23.3%.

In our approach we utilize an ETL interlayer composed of PCBM and ICBA, blended in various ratios, followed by thermally evaporated C_{60} . We chose this approach since evaporated C_{60} works well integrated into tandems, so we use the fullerene derivative blends to modify the ETL interface rather than completely replacing the ETL. The subsequent evaporated ETL also nearly eliminates the risk of pin-holes forming between the perovskite and the electrode. Neat ICBA should be preferable to neat PCBM as an ETL material for wide bandgap perovskites, since its lowest unoccupied molecular orbital (LUMO) is located closer to the vacuum level. However, despite delivering higher voltages when neat ICBA is used in solar cells, series resistance is significantly increased and overall efficiency reduced. Through investigating a thorough range of blend ratios, we find that with as little as 2% PCBM blended into ICBA, the high voltage is retained yet the series resistance is dramatically reduced. We rationalise these improvements through a detailed structural and electronic investigation of the blended fullerene layers and their impact on the optoelectronic properties of the solar cells.

Results & discussion

Our aim with implementing mixed PCBM and ICBA as a thin interlayer before the C₆₀ deposition (structures in Fig. 1a) in WBG PSCs (Fig. 1b) was to tune the energetic alignment between the lowest unoccupied molecular orbital (LUMO) of the two materials21-23 with the conduction band maximum (CBM) of the perovskite. We hypothesised that this may increase the $V_{\rm OC}$ while still utilizing evaporated C₆₀ as the main ETL. So, our first objective was to understand how the material properties changed when PCBM and ICBA were blended in varying proportions.

To first understand the electronic variation between the different PCBM: ICBA blends, we performed space-charge limited current (SCLC) measurements (Fig. 1c) on "electrononly" devices to determine the charge mobility in a perpendicular direction through the films (See Methods for details). Here we processed thicker fullerene layers than we use in the solar cells, with thicknesses between 75 and 85 nm (Fig. S1 and Table S1†) in order to avoid pin-holes and short-circuits. As we show in Fig. 1d, the extracted vertical electron mobility of PCBM and ICBA mixed 50:50 by mass increases by more than one order of magnitude, as compared to either neat PCBM or ICBA films. There is an increase in mobility compared to the neat materials across a full range of blend ratios as well, with a general decrease in mobility as ICBA concentration increases (Fig. S2, S3 and Table S2†). Surprisingly, however, when the ratio of PCBM is reduced to 2% by mass, we determine the highest mobility of any of the materials tested at 3.3×10^{-3} cm² V⁻¹ s⁻¹

Additionally, while neat PCBM and ICBA electron-only devices exhibit current-voltage (IV) characteristics consistent with an electric "field-dependent" mobility, we do not observe this characteristic in the 50:50 and 2:98 PCBM: ICBA blends.

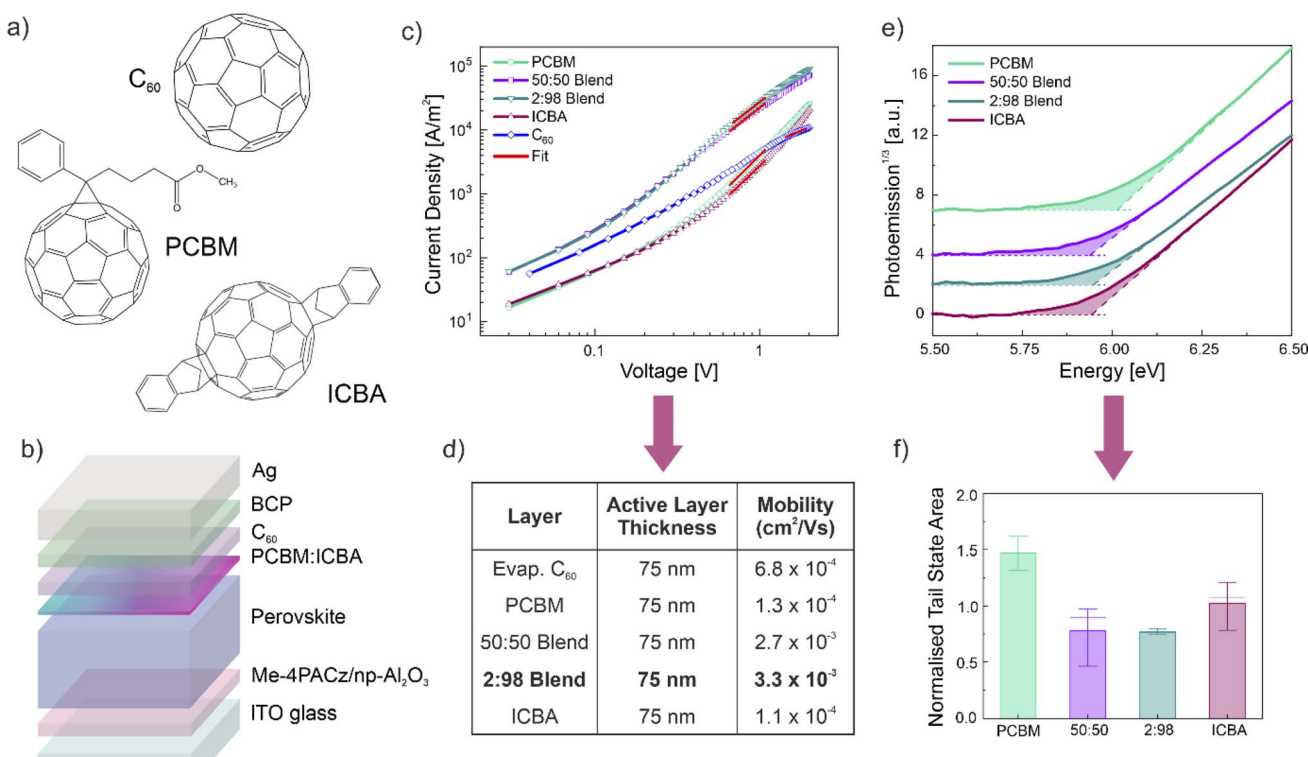


Fig. 1 Overview of material properties of PCBM: ICBA blends utilized in this work. (a) Chemical structures of C_{60} , PCBM, and ICBA. (b) Wide gap p-i-n device stack used in this work, featuring a PCBM: ICBA ETL interlayer. (c) Space-charge limited current (SCLC) measurement results of C_{60} vs. neat PCBM, ICBA and select blends as the active layer in electron-only devices (glass/Al/active layer/Ca/Al). (d) Table of mobility values fitted from SCLC measurements in part (c) for the different fullerene layers. (e) Atmospheric photoelectron spectroscopy (APS) results for PCBM, ICBA and select blend films on silicon substrates. (f) Normalized tail state areas of 3 repeat APS traces for each of the different fullerene films, means indicated by the middle horizontal crosshairs.

Neat PCBM and ICBA show trap-limited behaviour, therefore requiring to be fit with the Mott–Gurney equation modified for field-dependent mobility (eqn (1) in Methods). The blends exhibit characteristics of trap-free behaviour and no electric-filed dependency, as well as a negligible difference in mobility across a range of thicknesses (Fig. S1 and Table S1†).

This method of fitting allows us to extract the mobilities even though the measurement voltage is limited to 2 V and does not reach the trap-free region for all materials. Reaching beyond this voltage is difficult for organic materials in active layers below 100 nm, as the devices easily develop short-circuits even at moderate voltages. Additionally, the fact that we are not reaching trap-free SCLC for neat PCBM and ICBA in the same region of 50:50 and 2:98 blends confirms that the pristine materials have a hindered charge transport compared to the blends. If we could increase the voltage above 2 V and fit that region *via* eqn (1), we would still expect lower mobilities.

We also performed ambient photoemission spectroscopy (APS) measurements on thicker films (\sim 75 nm) of each material to observe the differences in energetics (Fig. 1e). With this technique we could determine if there are any changes in the energetic alignment between the WBG perovskite and a blend of PCBM and ICBA as explored in previous work. ^{21–23} To perform these measurements, the PCBM: ICBA films were illuminated

by a UV lamp with photon energies varying between 4.0 and 6.9 eV. The HOMO levels of the photogenerated electrons were then determined by fitting the linear region of the cube root of the generated photocurrent (see Methods for additional details).²⁷ We were able to verify with this technique that blending a PCBM into ICBA did not result in a major shift in the energy of the frontier orbitals. This implies that we would expect a similar energetic alignment between the ETL and the perovskite when using a blend with a small amount of PCBM, as with neat ICBA (Fig. S4 and S5†).

Additionally, by taking the tail state areas of the APS traces, we can quantify the energetic disorder in the films of the different materials.²⁸ Fig. 1f shows that the mean normalised tail state areas of the 50:50 and 2:98 blends are the lowest, with the lowest mean of 0.77 for the 2:98 blend from three repeat measurements. This indicates fewer sub-gap tail states and hence less electronic disorder than either neat PCBM or ICBA, which have mean normalised tail state areas of 1.47 and 1.02, respectively. This suggests that with the PCBM: ICBA blends there are fewer states available within the bandgap, and likely at the interface with the perovskite when integrated into devices. The reduced energetic disorder in the 2:98 blend also correlates with the improved mobility of the material (Fig. S6†).

Next we investigated the structural properties of mixed PCBM: ICBA films. To understand any possible structural variation between the different fullerene layers, we fabricated thicker (~75 nm) films of neat PCBM, ICBA, and blends with 50% and 2% PCBM by mass and conducted synchrotron grazing-incidence wide-angle X-ray scattering (GIWAXS) measurements (see Methods for further details).

For all samples, the 2D GIWAXS data (Fig. 2a-d) shows four broad Debye-Scherrer scattering rings at $q \approx 0.7, 1.35, 2.05$ and 3.1 \mathring{A}^{-1} , consistent with a weakly crystalline, partially disordered fullerene layer. ^{29,30} Comparing the highest intensity ring at $q \approx$ 1.35 Å^{-1} , this ring is broader and less intense for ICBA than PCBM, indicative of a more disordered or amorphous layer for ICBA.31 For the 2:98 PCBM: ICBA blend the ring is similarly broad to ICBA but with intensity comparable to PCBM, which indicates an enhancement in crystallinity of the layer.32 We analyse these differences in crystallinity further using 1D azimuthally integrated profiles of the 2D data (Fig. 2e), and quantify by fitting Pseudo-Voigt peaks to the scattering at $q \approx$ 1.35 Å^{-1} (all fitting results are shown in Table S3†). Across the investigated compositional range, we find the peak full-widthhalf-maxima (FWHM) increases with ICBA content, while the peak area trends lower to ICBA but with 2% PCBM as a clear outlier (Fig. S7a and b^{\dagger}). From the peak centre in q, we calculate the corresponding real space dimension d of the amorphous peak (Fig. S7c†). For PCBM this distance is 4.56 Å, and for ICBA 4.70 Å, but remarkably the 2:98 blend shows a contraction to

4.62 Å, indicating a significant reduction in the average fullerene-fullerene distance and closer spherical packing, as compared to the neat ICBA films.

We further conduct Scherrer analysis (see ESI Note 1†), considering the primary contribution to the peak broadening to be crystal domain size (neglecting disorder),31 and find a slight increase in the estimated coherent domain length from 1.44 nm for ICBA to 1.54 nm with 2% PCBM (Fig. S7d†). Taken together, the closer packing, higher intensity scattering and increased domain size point to an increase in overall crystallinity when a trace amount of PCBM is added to ICBA.33 Fig. 2f shows the results of atomic force microscopy-infrared spectroscopy (AFM-IR) measurements taken to determine the length scales of PCBM: ICBA mixing. We identified via an initial IR scan of the two neat materials (Fig. S8†) that the carbonyl (C=O) stretching band at 1735 cm⁻¹ uniquely identifies PCBM, so by mapping the absorption signal at this wavenumber we can understand the distribution of PCBM over the sample surface. As we progress from neat ICBA to neat PCBM the AFM-IR signal shown in Fig. 2f appears brighter with increasing PCBM concentration, as expected. When the absorption data across the spatial scans are collected by intensity and plotted in a histogram (Fig. S9†), we observe a clear trend of increasing overall absorption intensity with increasing PCBM concentration. The width of each histogram peak - corresponding to the variation in absorption intensity across each spatial scan - also remains relatively constant (Table S4†), and without any double peak features

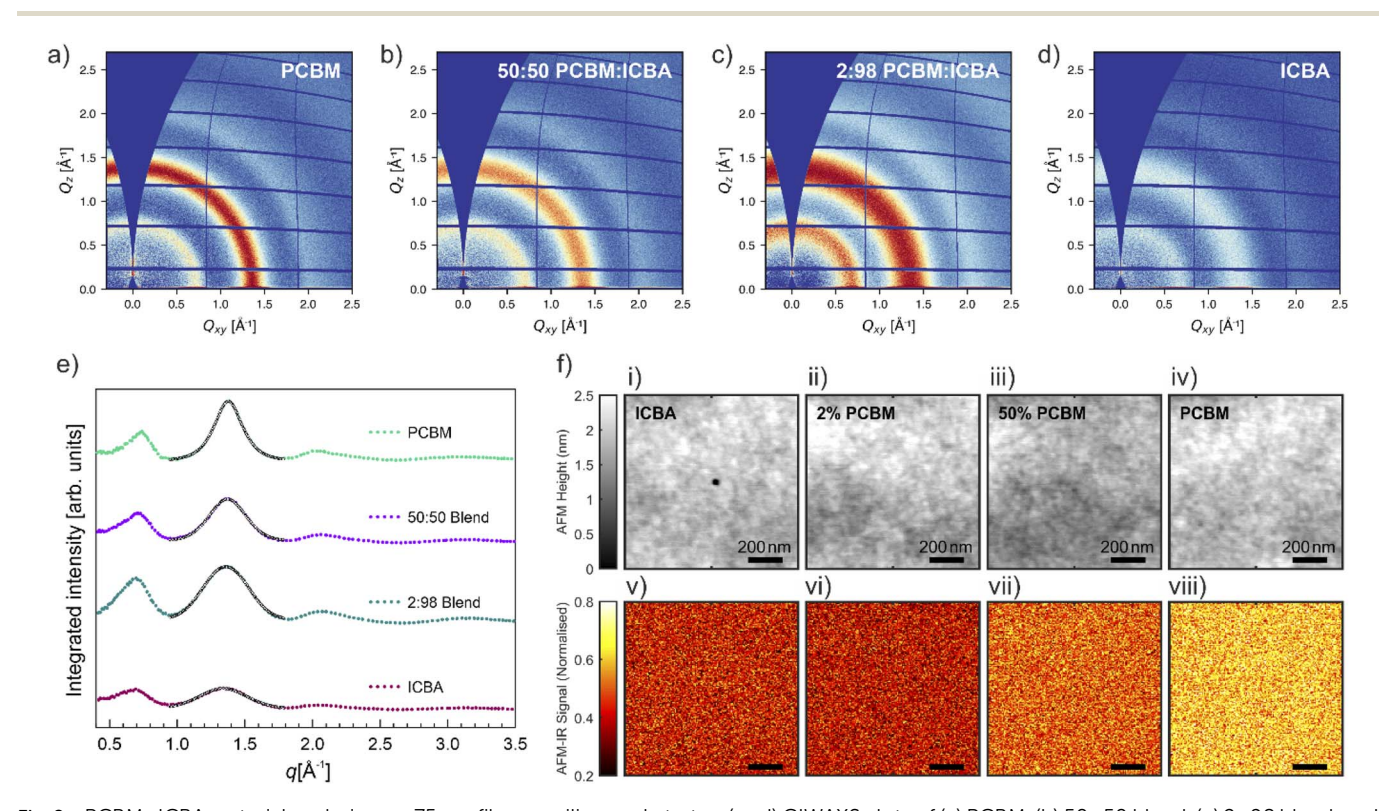


Fig. 2 PCBM: ICBA material analysis on \sim 75 nm films on silicon substrates. (a–d) GIWAXS plots of (a) PCBM, (b) 50:50 blend, (c) 2:98 blend, and (d) neat ICBA. (e) 1D integration of GIWAXS for the PCBM: ICBA materials, with peak fitting shown. (f) Atomic force microscopy-infrared spectroscopy (AFM-IR) scans of PCBM: ICBA films. (i-iv) show the AFM-IR height data, and (v-viii) show the intensity of the AFM-IR signal at 1735 cm⁻¹ wavenumber which is particular to PCBM.

Paper EES Solar

which would correspond to distinct PCBM-rich (high absorption) and PCBM-poor (low-absorption) domains (Fig. S9 \dagger). The AFM-IR therefore confirms that down to the \sim 20 nm resolution scale of the instrument there are not distinct domains of PCBM and ICBA, suggesting that the PCBM and ICBA are closely intermixed within the layer.

Previous work isolating the ICBA-tran3 isomer from assynthesized ICBA demonstrated that the isolated isomer material showed smaller energetic disorder and improved conductivity compared to the as-synthesized ICBA, without impacting the LUMO level.34 They suggested that the electronic disorder and molecular disorder are related, and the improved molecular ordering correlates with increased molecular packing and intermolecular π - π orbital overlapping to form effective charge transport channels in the material. From our APS and SCLC results in Fig. 1, coupled with the structural improvements discussed in Fig. 2, it appears that a similar improvement in packing and ordering is occurring within the 2:98 blend of PCBM and ICBA. Overall, the combination of increased electron mobility, high crystallinity, and reduced energetic disorder in the 2:98 PCBM:ICBA blend indicates a high quality ETL material. Importantly, the PCBM: ICBA blends also appear to be quite similar when deposited in thick vs. thin layers. UV-vis absorption traces of the materials do not show significant difference in shape between thick layers used for characterization and thin layers used in devices (Fig. S10†). SEM images of the fullerene blend layers show that the films appear to be quite smooth and homogeneous, when deposited both in thick and thin layers (Fig. S11†). This is maintained when the layers are deposited on top of perovskite as well (Fig. S12†). From this we move forward with the assumption that the material properties observed in the thicker layers provide useful insight into the impact the thin interalyers have on our solar cell devices.

We implemented thin PCBM: ICBA interlayers in 1.77 eV WBG perovskite solar cells (see Fig. S13† for bandgap determination via EQE), with a p-i-n structure as depicted in Fig. 1b. We investigated a range of blend ratios, to determine the optimal blend for peak device performance, and show the solar cell performance parameters in Fig. S14.† We observe a consistent trend of increasing $V_{\rm OC}$ with an increasing ratio of ICBA (after an initial $V_{\rm OC}$ drop from neat PCBM to 90% PCBM, which requires further investigation to explain), with the highest voltages reaching >1.30 V in devices with both 2:98 PCBM: ICBA and neat ICBA interlayers (Fig. S14a†). The $J_{\rm SC}$ remains relatively consistent across all blend ratios, only dropping significantly with neat ICBA (Fig. S14b†). The highest FF is seen with small amounts of PCBM in ICBA (Fig. S14c†). This is reflected in overall PCE and MPP data, with the best performing devices having a very small amount (2–5% by mass) of PCBM in ICBA (Fig. S14d and e[†]) consistent with the improved material properties previously discussed.

Photoluminescence (PL) images of devices were then taken across the range of PCBM: ICBA interlayer blends to quantify the impact upon quasi-Fermi level splitting (QFLS) (Fig. 3a) and investigate for inhomogeneities across the full 0.25 cm² device area (Fig. S15, ESI Note 2†).³⁵ The trend of increasing QFLS calculated from device photoluminescence quantum yield

(PLQY) closely follows that of increasing $V_{\rm OC}$ with increasing ICBA proportion (Fig. 3b) indicating that the additional and compositionally varied fullerene layer reduces the non-radiative losses at that interface.

Despite the high V_{OC} 's, shown in Fig. 3b, however, there is still a small gap (\sim 20 meV) between the QFLS and $V_{\rm OC}$ suggesting that the energetic alignment could still be improved. 9,10,12 Despite this misalignment, the $V_{\rm OC}$ we determine when we illuminate the cell without an optical mask reaches as high as 1.33 V for the 2:98 PCBM:ICBA interlayer device, which is shown in Fig. 3e. This higher $V_{\rm OC}$ under fullarea illumination practically eliminates the mismatch between the QFLS and $V_{\rm OC}$, suggesting that dark area losses are one possible cause of the disagreement between the measured $V_{\rm OC}$ and QFLS, which is an artifact of the measurement methodology, rather than a fundamental loss. The idea that minimal energetic mismatches are occurring during the operation of the cell is further supported by the determination of the nonradiative losses in a selection of blends (Fig. 3c). These results were determined from PLOY of device "half-stacks" fabricated without the final electrodes: Me-4PACz/perovskite film/PCBM: ICBA blend/C₆₀. These stacks had the highest losses with PCBM and the 50:50 blend, and the losses (calculated as QFLS rad -QFLS from the PL) were significantly reduced with smaller amounts of PCBM, reaching under 200 meV for the 2:98 blend. The average excited charge-carrier lifetime (determined by stretched exponential fitting of time-resolved luminescence) in similar half-stack samples (excluding C_{60}) increases significantly with the high proportion of ICBA, following the trend of improved QFLS, reaching 29 ns for the 2: 98 blend compared to 13 ns for neat PCBM and 19 ns for the 50: 50 blend (Fig. 3d and Table S5†). These charge-carrier lifetime results provide additional evidence of reduced interfacial recombination with the 2:98 PCBM:ICBA blend.

In addition to using the PL imaging to determine the QFLS, we can compare the difference between PLQY at open-circuit, to that under short-circuit conditions to determine an approximation of charge collection efficiency, which we term "charge collection quality" ($Q_{\rm col}$). The devices with neat PCBM and ICBA as well as the blends with higher proportions of ICBA generally showed a higher charge collection quality³⁵ (Fig. S16 and S17†) correlating with more efficient current extraction. The device with the 2:98 blend showed a dip in collection quality, however, that may be due to this particular device having poorer film uniformity (Fig. S16†).

WBG device results for the 2:98 PCBM: ICBA blend compared to each neat material as well as C_{60} alone as the ETL are shown in Fig. 4a–d for device areas of 0.25 cm² and 1 cm². The champion device using the 2:98 blend achieved a $V_{\rm OC}$ of 1.30, FF of 0.84, $J_{\rm SC}$ of 17.5 mA cm⁻², and a maximum power point (MPP) tracked PCE of 18.7% (Fig. 4a–d and S14†). The devices utilizing the blends with high ICBA concentrations also demonstrated the most reproducibility for each of the performance parameters (Fig. S14†), indicating that this method has the potential to be scaled-up.

Having identified the ideal ETL interlayer blend composition, we proceed to improve the PSC further by introducing

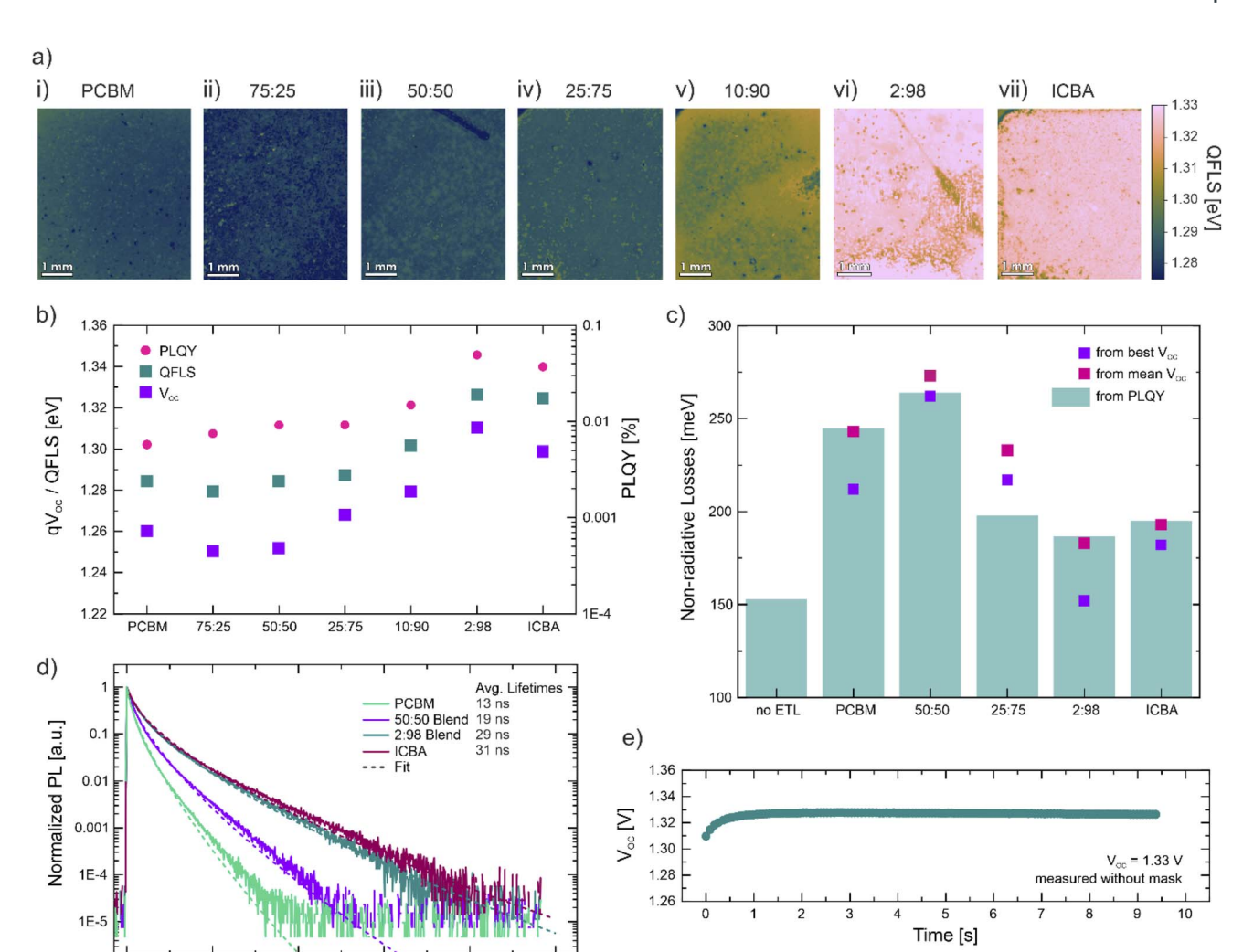


Fig. 3 Photoluminescence (PL) characterization of perovskite solar cells and half-stacks with PCBM: ICBA ETL interlayers to determine impact on non-radiative losses within the device. (a) Spatial maps of quasi-Fermi level splitting (QFLS) of complete solar cells with PCBM: ICBA interlayers (ITO/Me-4PACz/np-Al $_2$ O $_3$ /perovskite/PCBM: ICBA/C $_6$ 0/BCP/Ag). (b) Comparison of photoluminescence quantum yield (PLQY) & QFLS (average values from images), and $V_{\rm OC}$ (same imaged device measured under simulated AM1.5 100 mW cm $^{-2}$ irradiance) of complete solar cells with PCBM: ICBA interlayers. (c) Non-radiative losses of solar cell half-stacks with PCBM: ICBA interlayers (ITO/Me-4PACz/np-Al $_2$ O $_3$ /perovskite/PCBM: ICBA/C $_6$ 0) calculated from measured $V_{\rm OC}$ and average PLQY from images. (d) Time-resolved photoluminescence with stretched exponential fitting of half-stacks with PCBM: ICBA interlayers (ITO/Me-4PACz/perovskite/PCBM: ICBA). (e) Steady state $V_{\rm OC}$ of complete solar cell with 2:98 PCBM: ICBA interlayer.

additional passivation at this interface. We combine the 2:98 PCBM: ICBA interlayer with 1,3-propane-diammonium iodide (PDAI₂) surface passivation³⁶ and observe additional performance enhancements. The champion device shown in Fig. 4e and f devices had an added layer of PDAI₂ (and atomic layer deposited SnO₂ rather than BCP to utilize an architecture suitable for all-perovskite tandems), and had an increased gain in $V_{\rm OC}$ to reach 1.33 V (with optical shadow masking) and in PCE to reach 19.9%, with MPP PCE of 19.5%. The losses relative to the radiative limit for the champion 1.77 eV device with both passivation and the PCBM: ICBA interlayer compared to the champion reference (no passivation or interlayer) is shown in Fig. 4g and h. Both the $V_{\rm OC}$ and FF of these devices reached within 10% of the radiative limit. It is notable, however, that the

200

400

Time from Pulse [ns]

un-passivated devices performed nearly as well, as did the passivated devices with no PCBM: ICBA interlayer (Fig. S18†). This indicates that similar improvement in the measured $V_{\rm OC}$ comes from the ETL bilayer and passivation. The combination of these strategies does, however, show an improvement in the reproducibility of the high device performance (Fig. S18†).

We finally investigated if this ETL interlayer strategy could be applied across different bandgaps and different device stacks. PSCs with a $FA_{0.83}Cs_{0.17}Pb(I_{0.9}Br_{0.1})_3$ perovskite layer and 1.6 eV bandgap passivated with ethylene-diammonium diiodide $(EDAI_2)^{37}$ were fabricated based on a recently reported method. The highest efficiency 1.6 eV devices, with the same ETL stack as the 1.77 eV devices (PCBM: ICBA/C₆₀/BCP/Ag), utilized a 25:75 PCBM: ICBA blend, chosen by investigating a range of blend

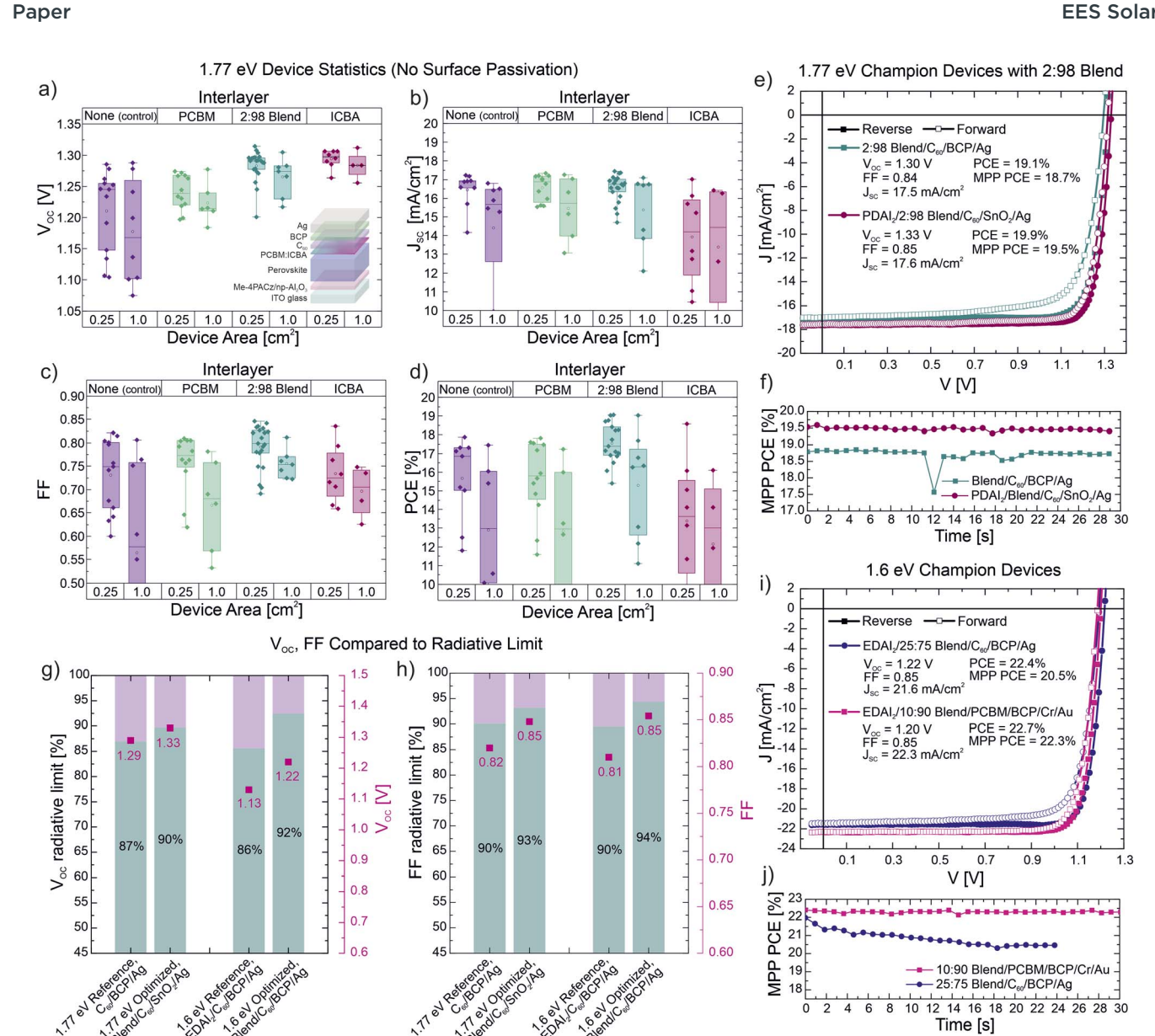


Fig. 4 Device results utilizing the optimized PCBM: ICBA ETL interlayer. (a-d) Device performance statistics [V_{OC} (a), J_{SC} (b), FF (c), PCE (d)] for 1.77 eV perovskite solar cells (ITO/Me-4PACz/Al₂O₃ np/perovskite/PCBM: ICBA/C₆₀/BCP/Aq) with no ETL interlayer, neat PCBM, the optimized 2:98 PCBM: ICBA blend, and neat ICBA interlayers. (e) JV curves of champion 1.77 eV perovskite solar cell with 2:98 PCBM: ICBA interlayer (blue), and with addition of PDAI₂ surface passivation (pink). Note that the devices with PDAI₂ passivation also use SnO₂ rather than BCP. (f) 30 seconds max power point tracking of the 1.77 eV champion 2:98 blend devices. (g) Percentage of the radiative limit and values of the champion device V_{OC} for reference devices (no surface passivation, no fullerene interlayer) and optimized devices with surface passivation and fullerene interlayer with 1.77 eV and 1.6 eV bandgaps [1.6 eV results from blue curve architecture (ITO/Me-4PACz/Al₂O₃ np/perovskite/EDAl₂/PCBM: $ICBA/C_{60}/BCP/Ag$) in (i) for comparison with 1.77 eV architecture]. (h) Percentage of the radiative limit and values of the champion device FF for control devices and optimized devices with surface passivation and fullerene interlayer with 1.77 eV and 1.6 eV bandgaps [1.6 eV results again from blue curve in (i)]. (i) JV curves of champion 1.6 eV perovskite solar cells using PCBM: ICBA interlayers in two device stacks (after the EDAI₂ surface passivated perovskite) – the blue curve with 25:75 PCBM: ICBA interlayer/ C_{60} /BCP/Ag, and the pink curve with 10:90 PCBM: ICBA interlayer/PCBM/BCP/Cr/Au. (j) 30 seconds max power point tracking of the 1.6 eV champion devices.

ratios similar to those used in the wider bandgap devices (Fig. S19†). In the champion device with this stack, we observe improved performance in the JV (Fig. 4i, blue curve). The champion device $V_{\rm OC}$ improved from 1.13 in the control to 1.22 V in the device with the interlayer, only 6% away from the radiative $V_{\rm OC}$ limit for this bandgap (Fig. 4g). We also reach a FF of 0.85, which is within 6% of the radiative limit for FF for this bandgap (Fig. 4h). The PCBM: ICBA interlayer was also applied in an alternative ETL stack for this bandgap (PCBM: ICBA/ PCBM/BCP/Cr/Au), recently reported by Gallant et al.,38 and

again shows improved performance (Fig. 4i, pink curve) with an optimized blend of 10:90 PCBM: ICBA (Fig. S20†). With this stack, the $V_{\rm OC}$ did not improve as much but the overall performance reached 22.7%, with an improved MPP PCE of 22.3% (Fig. 4j). This variation of the architecture for the 1.6 eV bandgap also shows reduced hysteretic losses. Though the mechanism for the change in optimum PCBM: ICBA content is not fully understood and requires more thorough investigation, all these devices with varying architectures show promising results and indicate exciting potential to extend this approach to other PSC systems.

Conclusions

Reducing losses in open-circuit voltage is one of the primary remaining challenges for wide bandgap perovskite solar cells. In this work we were able to reduce these losses in 1.77 eV bandgap devices by utilizing an electron transport layer composed of a thin interlayer of 2:98 mass ratio PCBM:ICBA followed by thermally evaporated C₆₀. We were able to achieve a $V_{\rm OC}$ of 1.33 V in addition to a very high fill factor of 0.85 resulting in a steady state PCE of 19.5%, without compromising the J_{SC} (17 mA cm⁻²), which is likely due to the improved crystallinity and enhanced charge carrier mobility in the blended fullerene layer. The optimized 2:98 blend samples achieved an order of magnitude higher mobility than films of either neat material, and the QFLS in devices increased from 1.28 V with neat PCBM to 1.33 V for the blend, indicating reduced nonradiative recombination at the ETL interface. Our results suggest that the quality of electron transport materials can be improved via further investigation of crystallizing agents, or precise ratios of other commonly used charge transport materials to take advantage of synergistic effects and the beneficial properties of each. We believe that this strategy of finely tuning fullerene interlayers could be more widely applicable to other perovskite compositions and solar cell stacks. The interlayer compositional tuning technique presented here has great, unexplored potential for improving the performance of a wide range of perovskite-based devices, and could prove extremely promising in the scaling up of perovskite photovoltaic technologies.

Experimental methods

Materials

Substrates. Patterned ITO substrates for solar cell fabrication were purchased from Biotain. Silicon wafers used for GIWAXS and APS samples were from LG Siltron.

Solvents. All solvents used in this work were purchased from Merck and used as delivered.

Fullerene interlayer materials. PCBM was purchased from Solenne & Ossila, and ICBA was purchased from Merck. Both materials were used as delivered.

Perovskite precursors. FAI was purchased from Greatcell Solar Materials, CsI and PbBr₂ were purchased from Alfa Aesar, and PbI2 was purchased from TCI. All were used as delivered.

Passivation materials. PDAI₂ was purchased from Greatcell Solar Materials, and EDAI2 was purchased from Merck. Both were used as delivered.

Transport layers. Me4-PACz was purchased from TCI. Al₂O₃ nano-particles (<50 nm particle size, 20 wt% in IPA) used for the wetting layer were purchased from Merck. Both were used as delivered. C₆₀ (>99.95% purity) was purchased from Creaphys, BCP was purchased from Merck, and Ag was purchased from Testbourne for use in the National Thin Film Cluster Facility.

Sample fabrication

Films for APS, GIWAXS, and AFM-IR. Si wafer substrates were scrubbed with decon soap and then underwent 15 minutes of ultrasonic cleaning each in decon, de-ionized water, acetone, and isopropyl alcohol. Then \sim 75 nm thick films of PCBM : ICBA were prepared by spin-coating 20 mg mL⁻¹ of the desired mass ratios in 9:1 chlorobenzene:dichlorobenzene at 700 rpm for 20 seconds, before annealing at 100 °C for 3 minutes.

Perovskite solar cells. This work was primarily done on 1.77 eV bandgap devices, with a perovskite composition of $FA_{0.83}Cs_{0.17}Pb(I_{0.6}Br_{0.4})_3$. The perovskite solution of 411.5 mg FAI, 127.2 mg CsI, 531.0 mg PbI₂, and 634.3 mg PbBr₂ was dissolved in a 4:1 volumetric ratio of DMF: DMSO to a concentration of 1.2 M. The solution was placed on a magnetic stir plate with a stir bar to stir overnight.

Prepatterned indium-doped tin oxide (ITO) coated glass substrates were scrubbed with decon soap and then underwent 15 minutes of ultrasonic cleaning each in decon, de-ionized water, acetone, and isopropyl alcohol. The substrates then underwent a 30-minute UV-O₃ treatment immediately before device fabrication. 200 µL of self-assembled monolayer Me-[4-[(3,6-dimethyl-9*H*-carbazol-9-yl)butyl]phosphonic 4PACz acid] solution (0.33 mg mL⁻¹ in anhydrous ethanol) was then deposited in an N2 glovebox. The solution was deposited onto the substrate, and then after 10 seconds spun at 3000 rpm for 20 seconds with an acceleration of 600 rpm s^{-1} . This layer was then annealed for 10 minutes at 100 °C in the same environment. After the Me-4PACz coated substrates cooled, 70 µL of Al₂O₃ nanoparticles (1:150 alumina nanoparticles: isopropanol) was deposited dynamically at 6000 rpm for 30 seconds (2000 rpm s^{-1}), and annealed at 100 °C for 1 minute. We have included this layer in the p-i-n device architecture in response to the poor wettability of perovskite solutions on some carbazolebased SAMs, as has been reported elsewhere.39 The use of Al₂O₃ nanoparticles in this way forms a thin mesoporous layer on top of the SAM, improving wettability.

For the 1.77 eV absorber layer, the previously made perovskite solution was first filtered through a 0.45 μm PTFE filter. 180 µL of the solution was then deposited dynamically, using a two-step spin coating method. The first step lasted 10 seconds with a speed of 1000 rpm and acceleration of 200 rpm s⁻¹, and the second step was 35 seconds with a speed of 6000 rpm and acceleration of 1000 rpm s^{-1} . The perovskite solution was deposited 7 seconds into the first step, followed by a 300 µL ethyl acetate antisolvent quench 35 seconds after the perovskite (42 seconds into the overall program). The perovskite was then

Paper

annealed for 30 minutes at 100 °C. For PDAI₂ passivated films, PDAI₂ solution (0.6 mg mL⁻¹ in 1:1 isopropanol:chlorobenzene by volume) was then spin-coated dynamically at 4000 rpm for 20 seconds and then annealed at 100 °C for 5 minutes.

The FA_{0.83}Cs_{0.17}Pb(I_{0.9}Br_{0.1})₃ 1.6 eV devices were processed according to the procedure used by Gallant et al. 38 In contrast to the 1.77 eV devices, these were fabricated on fluorine-doped tin oxide (FTO) coated glass substrates rather than ITO, and used MeO-2PACz ([2-(3,6-dimethoxy-9*H*-carbazol-9-yl)ethyl] phosphonic acid) instead of Me-4PACz. For the EDAI2 passivation, the solution of 325 µL of EDAI₂ (0.5 mg mL⁻¹ in 1:1 isopropanol: toluene by volume) was deposited on the previously deposited perovskite layer, and the substrate immediately spun at 3000 rpm (1333 rpm s^{-1}) to remove excess solution. The substrate was immediately annealed for 10 minutes at 100 °C in the same environment. EDAI2 surface treatment has previously been reported as a highly effective strategy for improving both the $V_{\rm OC}$ and operational stability of PSCs.³⁷

The final solution processed step for both the 1.77 eV and the 1.6 eV devices was the PCBM: ICBA solution, the desired mass ratios prepared from 5 mg per mL solutions of PCBM and ICBA in 9:1 chlorobenzene: dichlorobenzene (CB: DCB). 50 μL of the PCBM:ICBA solution was dynamically deposited at 2000 rpm for 20 seconds with an acceleration of 2000 rpm s⁻¹ and then annealed at 100 °C for 3 minutes. After the solution processing, 20 nm C₆₀, 5 nm bathocuproine (BCP), and 100 nm Ag were thermally evaporated in the National Thin-Film Cluster Facility with the exception of the 1.77 eV devices passivated with PDAI₂. These devices had SnO₂ rather than BCP, deposited via atomic layer deposition at a temperature of 100 °C, also in the National Thin-Film Cluster Facility.

For the second 1.6 eV PSC architecture, devices were completed with solution processed PCBM, BCP, and an evaporated CrAu electrode. The substrate was allowed to cool after the PCBM: ICBA interlayer processing, then 200 µL of PC₆₀BM solution (20 mg mL⁻¹ in 3:1 CB:DCB) was deposited on the substrate and allowed to spread for 10 seconds,39 before being spin coated at 2000 rpm (2000 rpm s⁻¹). The substrate was then annealed at 100 °C for 5 minutes in the same environment. Finally, once the substrates had cooled, the BCP solution (100 μ L) was spin coated dynamically at 5000 rpm (5000 rpm s⁻¹), and the substrate annealed at 100 °C for 2 minutes in the same environment. Using a chromium-coated tungsten bar, 3.5 nm of chromium was deposited on top of the substrate at a rate of 0.2 A s⁻¹, followed immediately by 100 nm of gold, which was evaporated on top of the substrates at an initial rate of 0.1 A s⁻¹ (to 5 nm, then ramped gradually to 1.2 A s⁻¹), all at a pressure < 2×10^{-6} torr.

Mobility measurements

Experimental procedure. Electron only devices were fabricated onto patterned bare glass, previously cleaned in detergent and water, and then ultrasonicated in acetone and isopropyl alcohol for 15 min each. The device structure employed is glass/ Al/active layer/Ca(10 nm)/Al. All active layer thin films are deposited in inert conditions in CB: DCB 9:1 at a spin speed of

1 krpm. Calcium (Ca-10 nm) and aluminum (Al-100 nm) were then deposited by evaporation through a shadow mask giving with pixel areas of 0.045 cm². Active layer thicknesses were measured with a dektak profilometer.

SCLC results-calculated mobilities. To fit the *J–V* curves the Mott-Gurney equation modified for the field-dependent mobility (eqn (1)) is employed:

$$J = \frac{9}{8} \varepsilon \varepsilon_0 \mu_0 \frac{(V - V_{bi})^2}{L^3} \exp\left(0.89 \gamma \sqrt{\frac{V - V_{bi}}{L}}\right) \tag{1}$$

where ε is the relative dielectric constant of the material (3 was assumed), ε_0 the vacuum permittivity, μ_0 the zero-field mobility, $V_{\rm bi}$ the built-in potential resulting from the work function difference of the electrodes, L the film thickness, γ is the field activation factor of mobility, and V is the applied voltage corrected for the voltage drop across the series resistance due to contacts. When extracting the values of μ_0 and γ from the experimental data, the value of μ at any field E can be obtained by using the Poole-Frenkel expression (eqn (2)):

$$\mu = \mu_0 \exp\left(\gamma \sqrt{E}\right) \tag{2}$$

APS and Kelvin probe measurements

Ambient photoemission spectroscopy (APS) and Kelvin Probe measurements were carried out using a KP Technology APS04 system. For APS measurements the samples, ~75 nm thick PCBM: ICBA layers on Si, were illuminated by a UV lamp fitted with a monochromator and the photon energy varied between 4.0 and 6.9 eV. Photogenerated electrons were detected using a Kelvin probe tip (ϕ : 2 mm, Au) positioned close (\sim 1 mm) to the surface and biased at +10 V. HOMO levels were determined by fitting the linear region of the cube root of the photocurrent through the Kelvin probe tip.27 For Kelvin probe measurements the same tip was used, which was calibrated prior to measurement using a cleaned Ag reference sample. The contact potential difference between the sample and the tip was allowed to equilibrate (\sim 60 min) before the final work function value was calculated.

GIWAXS measurements

Grazing-incidence wide-angle X-ray scattering (GIWAXS) data was acquired at the I07 beamline at Diamond Light Source. Monochromatic X-rays with energy 10 keV were incident on samples in air at grazing incidence angles $\alpha_i = 0.01$ – 0.3° collected in 0.01° steps. Scattering was collected by a Pilatus 2 M (DECTRIS) hybrid photon-counting detector with a sample-todetector distance (SDD) of 376.6 mm, with the experimental geometry calibrated using LaB6. Data was reduced and reshaped into q-space using scripts based on the pyFAI and pygix libraries. 30 Presented 1D data were acquired close to the critical angle (θ_c) , typically 0.16–0.19°, for maximum intensity from the sample and minimal substrate contribution (which dominates at $\alpha_i > \theta_c$). Background scatter from the substrate and air were subtracted from both the 1D and 2D data using data acquired on the same sample at $\alpha_i < \theta_c$. All 1D peak fitting was applied in Origin for the Scherrer analysis (see ESI Note 2, Table S3†).

EES Solar Paper

AFM-IR measurements

Atomic force microscopy-infrared spectroscopy (AFM-IR) works by utilising AFM techniques to measure the thermal expansion of the sample material upon absorption of infrared light. 40 The AFM-IR data presented in Fig. 2 of the main manuscript and Fig. S8 and S9 of the ESI† were taken using a neaSCOPE instrument from attocube systems AG. The AFM was operated in tapping mode at the first eigenmode of the AFM cantilever (80-85 nm tapping amplitude, 81 kHz tapping frequency, ARROW-EFM cantilevers from NanoWorld, tip radius roughly 20 nm). Simultaneously, infrared light from a pulsed laser (MIRcat-QT from Daylight Solutions) was directed onto the tip, with the laser pulse frequency being tuned to the difference between first (81 kHz) and second (570 kHz) cantilever eigenmodes (heterodyne tapping-mode AFM-IR). Pulsing the laser at this frequency induces a tip-enhanced thermal expansion of the sample, causing the sample to absorb the light, heat up, expand, cool, and contract over one laser cycle. This expansion cycle provides a driving force to the AFM and could be therefore detected. Stronger signals are attributed to stronger sample absorption, although we note other factors could play a role, such as optical gradient forces which are however typically small in organic samples.40,41 AFM-IR measurements were initially made of neat PCBM and ICBA films (referenced to a measurement of plain ITO glass to account for changes in the laser output power) as the laser output was tuned across a wide wavenumber range (900-1950 cm⁻¹) in order to locate the 1735 cm⁻¹ resonance associated with the PCBM (data values were subjected to moving average filter of ten data points). Once located, spatial scans of several PCBM: ICBA blended films were performed with the illumination wavelength fixed at 1735 cm⁻¹. AFM-IR data values were normalized by a global factor such that the maximum recorded data value for the neat PCBM film was set to 1.

Photoluminescence & QFLS images

Spatial PL and QFLS maps of devices were obtained using an inhouse constructed photoluminescence imaging setup. The setup contains an LED illumination source, a camera to collect and measure the PL, and a source meter to bias the sample. The devices were illuminated with a 450 nm LED (ThorLabs M450LP1) collimated by a Thorlabs SM2F lens, with the intensity set to 1 sun equivalent based on the short-circuit current. The PL was then detected by an ANDOR Zyla 4.2 camera under bias conditions set by a Keithley 2400.11,27 See ESI Note 1† for more details on setup and analysis.

TRPL measurements

Time-resolved photoluminescence measurements were carried out using a PicoQuant FluoTime 300 system. The sample were illuminated with a 505 nm laser and the PL was tracked at 720 nm (at the PL peak of the sample). The results were fit with a stretched exponential model to extract the characteristic and average decay times. A summary of the lifetimes for each sample is shown in Table S5.†

IV measurements

For IV measurements the area of the solar cell was masked to either 0.25 cm² or 1 cm². V_{OC} , J_{SC} , and MPP conditions were measured using a Keithley 2400 in ambient conditions under AM1.5 G irradiance generated by a Wavelabs SINUS-220 solar simulator. IV scans were performed at a rate of 0.3 V s⁻¹, from short-circuit to forward bias for the forward scans and from forward bias to short circuit for the reverse scans.

Data availability

Data for this article are available at the Oxford University Research Archive, at https://ora.ox.ac.uk/. The code for PL imaging equipment control, and analysis of PL imaging to generate QFLS and Qcol maps, both created by Akash Dasgupta, can be found on GitLab at https://gitlab.com/podgroup/pl-imaging-control and https://gitlab.com/pod-group/ PL_imaging_analysis. The code for stretched exponential fitting of TRPL, created by Manuel Kober-Czerny, can be found on GitHub at https://github.com/manuelkoberczerny/ fitting TRPL data. The code for analysis of JV data for solar cells, created by Akash Dasgupta, can be found on GitLab at https://gitlab.com/pod-group/

Akashs_amazing_analysis_automation.

Conflicts of interest

HJS is cofounder and chief scientific officer of Oxford PV Ltd, a company industrialising perovskite PV technology. The remaining authors declare no competing interests.

Acknowledgements

This work was part funded by the Deutsche Forschungsgemeinschaft (DFG, German Research Foundation), project number 424709669—SPP 2196 (HIPSTER-PRO), and the Engineering and Physical Science Research Council (EPSRC), UK, through the ATIP (Application Targeted and Integrated Photovoltaics) Programme Grant (EPSRC EP/T028513/1). We acknowledge Diamond Light Source for time on beamline 107 under proposal SI33462-1 for the GIWAXS measurements and thank Dr Daniel Toolan, Dr Rachel Kilbride, Dr Francesco Carla and Dr Jonathan Rawle for assistance with these experiments. We acknowledge the EPSRC National Thin-Film Cluster Facility for Advanced Functional Materials (NTCF), hosted by the Department of Physics at the University of Oxford, and Dr Jin Yao, the facility manager, for his support. The NTCF was funded by EPSRC (EP/M022900/1), the Wolfson Foundation and the University of Oxford.

References

1 Y. Zheng, Y. Li, R. Zhuang, X. Wu, C. Tian, A. Sun, C. Chen, Y. Guo, Y. Hua, K. Meng, K. Wu and C. C. Chen, Towards 26% efficiency in inverted perovskite solar cells via interfacial flipped band bending and suppressed deep-level Paper

traps, Energy Environ. Sci., 2024, 17(3), 1153-1162, DOI: 10.1039/D3EE03435F.

- 2 Z. Liang, Y. Zhang, H. Xu, W. Chen, B. Liu, J. Zhang, H. Zhang, Z. Wang, D. H. Kang, J. Zeng, X. Gao, Q. Wang, H. Hu, H. Zhou, X. Cai, X. Tian, P. Reiss, B. Xu, T. Kirchartz, Z. Xiao, S. Dai, N. G. Park, J. Ye and X. Pan, Homogenizing out-of-plane cation composition perovskite solar cells, Nature, 2023, 624, 557-563, DOI: 10.1038/s41586-023-06784-0.
- 3 C. Liu, Y. Yang, H. Chen, J. Xu, A. Liu, A. S. R. Bati, H. Zhu, L. Grater, S. S. Hadke, C. Huang, V. K. Sangwan, T. Cai, D. Shin, L. X. Chen, M. C. Hersam, C. A. Mirkin, B. Chen, M. G. Kanatzidis and E. H. Sargent, Bimolecularly passivated interface enables efficient and stable inverted perovskite solar cells, Science, 2023, 382(6672), 810-815, DOI: 10.1126/science.adk1633.
- 4 G. E. Eperon, S. D. Stranks, C. Menelaou, M. B. Johnston, L. M. Herz and H. J. Snaith, Formamidinium lead trihalide: a broadly tunable perovskite for efficient planar heterojunction solar cells, Energy Environ. Sci., 2014, 7(3), 982-988, DOI: 10.1039/C3EE43822H.
- 5 G. E. Eperon, M. T. Hörantner and H. J. Snaith, Metal halide perovskite tandem and multiple-junction photovoltaics, Nat. Rev. Chem., 2017, 1(0095), DOI: 10.1038/s41570-017-0095.
- 6 E. Aydin, T. G. Allen, M. De Bastiani, A. Razzaq, L. Xu, E. Ugur, J. Liu and S. De Wolf, Pathways toward commercial perovskite/silicon tandem photovoltaics, Science, 2024, 383(6679), DOI: 10.1126/science.adh3849.
- 7 S. Hu, J. Wang, P. Zhao, J. Pascual, J. Wang, F. Rombach, A. Dasgupta, W. Liu, M. A. Truong, H. Zhu, M. Kober-Czerny, J. N. Drysdale, J. A. Smith, Z. Yuan, G. J. W. Aalbers, N. R. M. Schipper, J. Yao, K. Nakano, S. H. Turren-Cruz, A. Dallman, M. G. Christoforo, J. M. Ball, D. P. McMeekin, K. A. Zaininger, Z. Liu, N. K. Noel, K. Tajima, W. Chen, M. Ehara, R. A. J. Janssen, A. Wakamiya and H. J. Snaith, Steering perovskite precursor solutions for multijunction photovoltaics, Nature, 2025, 639, 93-101, DOI: 10.1038/s41586-024-08546-y.
- 8 Z. Liu, R. Lin, M. Wei, M. Yin, P. Wu, M. Li, L. Li, Y. Wang, G. Chen, V. Carnevali, L. Agosta, V. Slama, N. Lempesis, Z. Wang, M. Wang, Y. Deng, H. Luo, H. Gao, U. Rothlisberger, S. M. Zakeeruddin, X. Luo, Y. Liu, M. Grätzel and H. Tan, All-perovskite tandem solar cells achieving >29% efficiency with improved (100) orientation in wide-bandgap perovskites, Nat. Mater., 2025, 24, 252-259, DOI: 10.1038/s41563-024-02073-x.
- 9 P. Caprioglio, J. A. Smith, R. D. J. Oliver, A. Dasgupta, S. Choudhary, M. D. Farrar, A. J. Ramadan, Y. H. Lin, M. G. Christoforo, J. M. Ball, J. Diekman, J. Thiesbrummel, K. A. Zaininger, X. Shen, M. B. Johnston, D. Neher, M. Stolterfoht and H. J. Snaith, Open-circuit and shortcircuit loss management in wide-gap perovskite p-i-n solar cells, Nat. Commun., 2023, 14, 932, DOI: 10.1038/s41467-023-36141-8.
- 10 M. Stolterfoht, P. Caprioglio, C. M. Wolff, J. A. Márquez, J. Nordmann, S. Zhang, D. Rothhardt, U. Hörmann, Y. Amir, A. Redinger, L. Kegelmann, F. Zu, S. Albrecht,

- N. Koch, T. Kirchartz, M. Saliba, T. Unold and D. Neher, The impact of energy alignment and interfacial recombination on the internal and external open-circuit voltage of perovskite solar cells, Energy Environ. Sci., 2019, 12(9), 2778-2788, DOI: 10.1039/C9EE02020A.
- 11 C. M. Wolff, P. Caprioglio, M. Stolterfoht and D. Neher, Nonradiative Recombination in Perovskite Solar Cells: The Role of Interfaces, Adv. Mater., 2019, 31(52), 1902762, DOI: 10.1002/adma.201902762.
- 12 P. Caprioglio, M. Stolterfoht, C. M. Wolff, T. Unold, B. Rech, S. Albrecht and D. Neher, On the Relation between the Open-Circuit Voltage and Quasi-Fermi Level Splitting in Efficient Perovskite Solar Cells, Adv. Energy Mater., 2019, 9(33), 1901631, DOI: 10.1002/aenm.201901631.
- 13 L. Y. Chen, O. Sun, Y. M. Xie and M. K. Fung, A review: strategies for reducing the open-circuit voltage loss of wide-bandgap perovskite solar cells, Chem. Commun., 2025, 61(6), 1063-1086, DOI: 10.1039/D4CC05131A.
- 14 R. Li, B. Chen, N. Ren, P. Wang, B. Shi, Q. Xu, H. Zhao, W. Han, Z. Zhu, J. Liu, O. Huang, D. Zhang, Y. Zhao and Zhang, CsPbCl3-Cluster-Widened Bandgap Inhibited Phase Segregation in a Wide-Bandgap Perovskite and its Application to NiO-Based Perovskite/Silicon Tandem Solar Cells, Adv. Mater., 2022, 34(27), 2201451, DOI: 10.1002/adma.202201451.
- 15 H. Bi, Y. Fujiwara, G. Kapil, D. Tavgeniene, Z. Zhang, L. Wang, C. Ding, S. R. Sahamir, A. K. Baranwal, Y. Sanehira, K. Takeshi, G. Shi, T. Bessho, H. Segawa, S. Grigalevicius, Q. Shen and S. Hayase, Perovskite Solar Cells Consisting of PTAA Modified with Monomolecular Layer and Application to All-Perovskite Tandem Solar Cells with Efficiency over 25%, Adv. Funct. Mater., 2023, 33(32), 2300089, DOI: 10.1002/adfm.202300089.
- 16 A. Al-Ashouri, E. Köhnen, B. Li, A. Magomedov, H. Hempel, P. Caprioglio, J. A. Márquez, A. B. M. Vilches, E. Kasparavicius, J. A. Smith, N. Phung, D. Menzel, M. Grischek, L. Kegelmann, D. Skroblin, C. Gollwitzer, T. Malinauskas, M. Jošt, G. Matič, B. Rech, R. Schlatmann, M. Topič, L. Korte, A. Abate, B. Stannowski, D. Neher, M. Stolterfoht, T. Unold, V. Getautis and S. Albrecht, Monolithic perovskite/silicon tandem solar cell with >29% efficiency by enhanced hole extraction, Science, 2020, 370(6522), 1300-1309, DOI: 10.1126/science.abd4016.
- 17 H. Wang, C. Zhang, Y. Yao, C. Cheng and K. Wang, Non-Fullerene Organic Electron Transport Materials toward Stable and Efficient Inverted Perovskite Photovoltaics, Small, 2024, 20(43), 2403193, DOI: 10.1002/smll.202403193.
- 18 A. Al-Ashouri, A. Magomedov, M. Roß, M. Jošt, M. Talaikis, G. Chistiakova, T. Bertram, J. A. Márquez, E. Köhnen, E. Kasparavičius, S. Levcenco, L. Gil-Escrig, C. J. Hages, R. Schlatmann, B. Rech, T. Malinauskas, T. Unold, C. A. Kaufmann, L. Korte, G. Niaura, V. Getautis and S. Albrecht, Conformal monolayer contacts with lossless interfaces for perovskite single junction and monolithic tandem solar cells, Energy Environ. Sci., 2019, 12(11), 3356-3369, DOI: 10.1039/C9EE02268F.

19 J. Dagar, M. Fenske, A. Al-Ashouri, C. Schultz, B. Li, H. Köbler, R. Munir, G. Parmasivam, J. Li, I. Levine, A. Merdasa, L. Kegelmann, H. Näsström, J. A. Márquez, T. Unold, D. M. Többens, R. Schlatmann, B. Stegemann, A. Abate, S. Albrecht and E. Unger, Compositional and Interfacial Engineering Yield High-Performance and Stable p-i-n Perovskite Solar Cells and Mini-Modules, ACS Appl. Mater. Interfaces, 2021, 13(11), 13022–13033, DOI: 10.1021/acsami.0c17893.

- 20 J. Thiesbrummel, F. Peña-Camargo, K. O. Brinkmann, E. Gutierrez-Partida, F. Yang, J. Warby, S. Albrecht, D. Neher, T. Riedl, H. J. Snaith, M. Stolterfoht and F. Lang, Understanding and Minimizing V_{OC} Losses in All-Perovskite Tandem Photovoltaics, *Adv. Energy Mater.*, 2023, 13(3), 2202674, DOI: 10.1002/aenm.202202674.
- 21 D. B. Khadka, Y. Shirai, M. Yanagida, T. Noda and K. Miyano, Tailoring the Open-Circuit Voltage Deficit of Wide-Band-Gap Perovskite Solar Cells Using Alkyl Chain-Substituted Fullerene Derivatives, ACS Appl. Mater. Interfaces, 2018, 10(26), 22074–22082, DOI: 10.1021/acsami.8b04439.
- 22 Z. Liu, J. Siekmann, B. Klingebiel, U. Rau and T. Kirchartz, Interface Optimization via Fullerene Blends Enables Open-Circuit Voltages of 1.35 V in CH3NH3Pb(I0.8Br0.2)3 Solar Cells, *Adv. Energy Mater.*, 2021, 11(16), 2003386, DOI: 10.1002/aenm.202003386.
- 23 H. Sun, K. Xiao, H. Gao, C. Duan, S. Zhao, J. Wen, Y. Wang, R. Lin, X. Zheng, H. Luo, C. Liu, P. Wu, W. Kong, Z. Liu, L. Li and H. Tan, Scalable Solution-Processed Hybrid Electron Transport Layers for Efficient All-Perovskite Tandem Solar Modules, *Adv. Mater.*, 2024, 36(2), 2308706, DOI: 10.1002/adma.202308706.
- 24 Tokyo Chemical Industry UK Ltd, available from: https://www.tcichemicals.com/GB/en/, cited 2025 Jun 3.
- 25 Merck United Kingdom, Life Science Products & Service Solutions, available from: https://www.sigmaaldrich.com/ GB/en, cited 2025 Jun 3.
- 26 Ossila, Low Price Lab Equipment & Materials, available from: https://www.ossila.com/, cited 2025 Jun 3.
- 27 I. D. Baikie, A. Grain, J. Sutherland and J. Law, Near ambient pressure photoemission spectroscopy of metal and semiconductor surfaces, *Phys. Status Solidi C*, 2015, **12**(3), 259–262, DOI: **10.1002/2Fpssc.201400086**.
- 28 C. Labanti, J. Wu, J. Shin, S. Limbu, S. Yun, F. Fang, S. Y. Park, C. J. Heo, Y. Lim, T. Choi, H. J. Kim, H. Hong, B. Choi, K. B. Park, J. R. Durrant and J. S. Kim, Light-intensity-dependent photoresponse time of organic photodetectors and its molecular origin, *Nat. Commun.*, 2022, 13, 3745, DOI: 10.1038/s41467-022-31367-4.
- 29 A. J. Pearson, T. Wang, A. D. F. Dunbar, H. Yi, D. C. Watters, D. M. Coles, P. A. Staniec, A. Iraqi, R. A. L. Jones and D. G. Lidzey, Morphology Development in Amorphous Polymer:Fullerene Photovoltaic Blend Films During Solution Casting, *Adv. Funct. Mater.*, 2014, 24(5), 659–667, DOI: 10.1002/adfm.201301922.
- 30 T. Agostinelli, S. Lilliu, J. G. Labram, M. Campoy-Quiles, M. Hampton, E. Pires, J. Rawle, O. Bikondoa, D. D. C. Bradley, T. D. Anthopoulos, J. Nelson and

- J. E. Macdonald, Real-Time Investigation of Crystallization and Phase-Segregation Dynamics in P3HT:PCBM Solar Cells During Thermal Annealing, *Adv. Funct. Mater.*, 2011, 21(9), 1701–1708, DOI: 10.1002/adfm.201002076.
- 31 J. Rivnay, R. Noriega, R. J. Kline, A. Salleo and M. F. Toney, Quantitative analysis of lattice disorder and crystallite size in organic semiconductor thin films, *Phys. Rev. B*, 2011, 84(4), 045203, DOI: 10.1103/PhysRevB.84.045203.
- 32 Z. Yang, Y. Guo, H. Li, Y. Zhou, X. Zuo, Y. Yu, C. Pan, J. Strzalka, C. Y. Nam and M. H. Rafailovich, Roles of Interfacial Tension in Regulating Internal Organization of Low Bandgap Polymer Bulk Heterojunction Solar Cells by Polymer Additives, *Adv. Mater. Interfaces*, 2018, 5(15), 1800435, DOI: 10.1002/admi.201800435.
- 33 G. Paternò, A. J. Warren, J. Spencer, G. Evans, V. G. Sakai, J. Blumberger and F. Cacialli, Micro-focused X-ray diffraction characterization of high-quality [6,6]-phenyl-C₆₁-butyric acid methyl ester single crystals without solvent impurities, *J. Mater. Chem. C*, 2013, 1(36), 5619–5623, DOI: 10.1039/C3TC31075B.
- 34 Y. Lin, B. Chen, F. Zhao, X. Zheng, Y. Deng, Y. Shao, Y. Fang, Y. Bai, C. Wang and J. Huang, Matching Charge Extraction Contact for Wide-Bandgap Perovskite Solar Cells, Adv. Mater., 2017, 29(26), 1700607, DOI: 10.1002/adma.201700607.
- 35 A. Dasgupta, S. Mahesh, P. Caprioglio, Y. H. Lin, K. A. Zaininger, R. D. J. Oliver, P. Holzhey, S. Zhou, M. M. McCarthy, J. A. Smith, M. Frenzel, M. G. Christoforo, J. M. Ball, B. Wenger and H. J. Snaith, Visualizing Macroscopic Inhomogeneities in Perovskite Solar Cells, ACS Energy Lett., 2022, 7(7), 2311–2322, DOI: 10.1021/acsenergylett.2c01094.
- 36 H. Chen, A. Maxwell, C. Li, S. Teale, B. Chen, T. Zhu, E. Ugur, G. Harrison, L. Grater, J. Wang, Z. Wang, L. Zeng, S. M. Park, L. Chen, P. Serles, R. A. Awni, B. Subedi, X. Zheng, C. Xiao, N. J. Podraza, T. Filleter, C. Liu, Y. Yang, J. M. Luther, S. De Wolf, M. G. Kanatzidis, Y. Yan and E. H. Sargent, Regulating surface potential maximizes voltage in all-perovskite tandems, *Nature*, 2023, 613, 676–681, DOI: 10.1038/s41586-022-05541-z.
- 37 S. Hu, K. Otsuka, R. Murdey, T. Nakamura, M. A. Truong, T. Yamada, T. Handa, K. Matsuda, K. Nakano, A. Sato, K. Marumoto, K. Tajima, Y. Kanemitsu and A. Wakamiya, Optimized carrier extraction at interfaces for 23.6% efficient tin-lead perovskite solar cells, *Energy Environ. Sci.*, 2022, 15(5), 2096–2107, DOI: 10.1039/D2EE00288D.
- 38 B. M. Gallant, P. Holzhey, J. A. Smith, S. Choudhary, K. A. Elmestekawy, P. Caprioglio, I. Levine, A. A. Sheader, E. Y.-H. Hung, F. Yang, D. T. W. Toolan, R. C. Kilbride, K. A. Zaininger, J. M. Ball, M. G. Christoforo, N. K. Noel, L. M. Herz, D. J. Kubicki and H. J. Snaith, A green solvent enables precursor phase engineering of stable formamidinium lead triiodide perovskite solar cells, *Nat. Commun.*, 2024, 15, 10110, DOI: 10.1038/s41467-024-54113-4.
- 39 A. Al-Ashouri, M. Marčinskas, E. Kasparavičius, T. Malinauskas, A. Palmstrom, V. Getautis, S. Albrecht,

- M. D. McGehee and A. Magomedov, Wettability Improvement of a Carbazole-Based Hole-Selective Monolayer for Reproducible Perovskite Solar Cells, *ACS Energy Lett.*, 2023, **8**(2), 898–900, DOI: **10.1021/acsenergylett.2c02629**.
- 40 B. T. O'Callahan, J. Yan, F. Menges, E. A. Muller and M. B. Raschke, Photoinduced Tip-Sample Forces for
- Chemical Nanoimaging and Spectroscopy, *Nano Lett.*, 2018, **18**(9), 5499–5505, DOI: **10.1021/acs.nanolett.8b01899**.
- 41 J. Jahng, E. O. Potma and E. S. Lee, Nanoscale spectroscopic origins of photoinduced tip–sample force in the midinfrared, *Proc. Natl. Acad. Sci.*, 2019, **116**(52), 26359–26366, DOI: **10.1073/pnas.1913729116**.